Molecular Level Interpretation of Vibrational Spectra of Ordered Ice Phases

Daniel R. Moberg,[*,†] Peter J. Sharp,[†] and Francesco Paesani[*,†,‡,¶]

†*Department of Chemistry and Biochemistry,*
University of California, San Diego, La Jolla, California 92093, United States

‡*Materials Science and Engineering,*
University of California, San Diego, La Jolla, California 92093, United States

¶*San Diego Supercomputer Center,*
University of California San Diego, Jolla, California 92093, United States

E-mail: dmoberg@ucsd.edu; fpaesani@ucsd.edu

Abstract

We build on results from our previous investigation into ice I_h using a combination of classical many-body molecular dynamics (MB-MD) and normal mode (NM) calculations to obtain molecular level information on the spectroscopic signatures in the OH stretching region for all seven of the known ordered crystalline ice phases. The classical MB-MD spectra are shown to capture the important spectral features by comparing with experimental Raman spectra. This motivates the use of the classical simulations in understanding the spectral features of the various ordered ice phases in molecular terms. This is achieved through NM analysis to first demonstrate that the MB-MD spectra can be well recovered through the transition dipole moments and polarizability tensors calculated from each NM. From the normal mode calculations, measures of the amount of symmetric and antisymmetric stretching are calculated for each ice, as well as an approximation of how localized each mode is. These metrics aid in viewing the ice phases on a continuous spectrum determined by their density. As in ice I_h, it is found that most of the other ordered ice phases have highly delocalized modes and their spectral features cannot, in general, be described in terms of molecular normal modes. The lone exception is ice VIII, the densest crystalline ice phase. Despite being found only at high pressure, the symmetry index shows a clear separation of symmetric and antisymmetric stretching modes giving rise to two distinct features.

Introduction

Ice is a common occurrence in our everyday lives, and whether found at the surface of a frozen lake, falling from the sky in the form of snow, or in an ice cube in a glass, the water molecules are always arranged in a hexagonal structure. This hexagonal ice, known as ice I_h, is the most common phase of ice found on the Earth's surface and in its atmosphere as it is stable at ambient conditions. Under conditions of high pressure and/or low temperature, however, ice can transition to a number of other crystalline phases, each with their own unique structure.[1] These conditions occur naturally only in extreme locations, such as insides glaciers in Antarctica,[2,3] in the planet's upper atmosphere,[4,5] and on the icy moons and satellites across our solar system.[6,7] Thus, having a molecular level understanding of the crystalline ice phases is important to a range of fields spanning terrestrial and oceanic, to atmospheric, planetary, and interstellar research.

Since the discovery of ice II over a century ago,[8,9] when the naming scheme for future ice phases was first established, a total of 17 different crystalline ice phases have been identified. Each phase adheres to the Bernal-Fowler "ice rules",[10] where for every oxygen atom there are two hydrogen bonds being accepted and two hydrogen bonds being donated, forming a tetrahedral hydrogen bond network. These phases can be divided into two main categories based on whether the hydrogens atoms of their water molecules exhibit long range order, referred to as either proton ordered or proton disordered phases. There are at present six known ordered/disordered ice pairs: XI/I_h, IX/III, XIII/V, XV/VI, VIII/VII, and XIV/XII. The remaining crystalline ices include the ordered ice II with no known proton disordered counterpart phase and ice I_c and ice IV as the only proton disordered phases currently missing their corresponding counterparts.[11] Ice X is a special case and lone exception to the Bernal-Fowler rules, where increasing pressure on ice VIII or VII results in each hydrogen atom being shared evenly between two oxygen atoms. Within the past few years, two additional proton disordered ices have been formed through the process of emptying a type sII clathrate hydrate and a hydrogen-filled ice, resulting in ices XVI[12] and XVII,[13] respectively. Notably,

the different ice phases that meet with the phase boundary for liquid water are all proton disordered, showing a trend that with increased temperature and entropy effects, the ordered phases transform to their disordered counterparts before eventually transitioning to liquid.

Much research has been done to understand the structure of ice I_h due to its common occurrence in nature and importance to many fields. The oxygen atoms of ice I_h are arranged in the hexagonal 'wurtzite' crystal lattice[14] with the hydrogen atoms bonded randomly to ensure the oxygen atoms satisfy the aforementioned Bernal-Fowler ice rules. The hydrogen atoms, therefore, have no long range order, resulting in an infinite number of possible lattice configurations for ice I_h. By contrast, its proton ordered counterpart ice XI has a well-defined unit cell. While the crystal lattice structures for the oxygen atoms in both ice I_h and ice XI are identical, the ice XI hydrogen atoms are in fixed positions. This proton ordering results in a finite number of phonon mode vibrations, which have been calculated for the unit cell through computational methods.[15]

Vibrational spectroscopy[16–31] and diffraction[32–41] experiments have proven invaluable tools for understanding the complex molecular structures and hydrogen bonding networks of the various ice phases. The OH stretching region in particular, extending from 3000 cm^{-1} to 3800 cm^{-1}, provides a direct measure of the strength of the hydrogen bond network in an aqueous system. Experimental infrared[16,17,19,24,29] and Raman[18,20–23,25–28,30,31] spectroscopic studies have been used to characterize the ice phases for decades. As condensed phase computational methods have become more sophisticated, complimentary theoretical studies have also increasingly proven invaluable in both interpreting spectra and predicting structures and electrostatic properties.[30,42–53]

Complicating matters is water being a network composed almost entirely of hydrogen bonds. This results in a general lack of damping effects on intermolecular coupling that would be induced by the presence of heavier molecules, creating difficulties in both experimental and computational structural interpretations. This delocalization and strong intermolecular coupling also suggests that a simple assignment of vibrational modes to individual spectral

peaks in water and ice is not appropriate.[48,50,52,54,55] Recently, experimental and computational two dimensional IR (2DIR) spectroscopy studies have been used to disentangle some of the vibrational cross-couplings.[55–58] The extra frequency dimension of 2DIR spectra provides information on the couplings and dynamics of different modes. However, interpretation of the spectra is far from trivial. With more sophisticated methods for modeling water, computational investigations can better aid in interpreting the one and two dimensional IR and Raman spectra beyond the limits of experiment. Recent computational investigations into the ice phases have focused on spectroscopic interpretation,[30,51,52] energetics of phases[53] and competition between proton order and disorder,[59,60] the ferroelectricity (or lack thereof) of ice XI,[61] phase transitions and volume isotope effects,[49,62–64] phonon/normal mode calculations,[15,52,65–67] and the pressure dependence of proton hopping.[68]

It has recently been demonstrated that a rigorous representation of the water properties can be derived from many-body molecular dynamics (MB-MD) simulations performed with the MB-pol potential energy function.[69–71] MB-pol represents a highly accurate molecular model of water[72] and correctly predicts structural, thermodynamic, and dynamical properties as well as vibrational spectra of water from the gas to the condensed phase.[52,72–77] Small energy differences between different ice phases demonstrate the importance of an accurate determination of the underlying potential energy surface for a quantitative assignment of the relative stability of the different ice phases. MB-pol has accurately reproduced the lattice energies for the ordered ice phases with known experimental comparisons, and provided predictions for the remaining ordered phases yet to be measured experimentally.[53] In particular, MB-pol has shown excellent agreement with both ice I_h IR and Raman spectra[52] and the energies of the ordered ice phases.[53] In Ref. 52, it was argued that classical MD captures the same, though narrowed, vibrational features that quantum centroid molecular dynamics (CMD) simulations do for ice I_h. Owing to the excellent agreement between experiment and CMD simulations at 200 K, normal mode calculations were employed to further understand the spectral features.

Building off the work of Ref. 52, this study applies a similar MB-MD and normal mode treatment to the ordered ice phases. Classical MB-MD simulations in conjunction with normal mode calculations are used to gain a more complete molecular level understanding of the ordered ice phases and the observed spectral features in the OH stretching region. Ice I_h is used as a point of comparison for the disordered phases and the computational methods employed.

Computational details

All MD simulations were performed within the many-body molecular dynamics (MB-MD) formalism.[73] System sizes differed between ice phases, with ices I_h, XI, and XV having 360 molecules, IX having 324 molecules, VIII having 384 molecules, ice XIV having 540 water molecules, ice II having 768 water molecules, and ice XIII having 756 water molecules. The simulations were carried out using in-house software based on the DL_POLY_2.0 MD software,[78] modified to include the MB-pol PEF. The initial configurations were taken from previous trajectories carried out in the isobaric-isothermal (NPT) ensemble.[53] The equations of motion were propagated using the velocity Verlet algorithm and the temperature was controlled via Nosé-Hoover chains of four thermostats coupled to each degree of freedom.[79–81] A cutoff of 9 Å was used to calculate the short-range interactions, while the long-range electrostatic interactions were evaluated in reciprocal space using the Ewald summation technique. A time step of 0.2 fs was used in the MD simulations.

After 100 ps of equilibration in the canonical (NVT) ensemble, 5 independent trajectories for 100 K simulations and 1 trajectory for 10 K simulations of 100 ps each were simulated in the microcanonical (NVE) ensemble. From the classical MD NVE trajectories, classical spectra were calculated from the system dipole moment (for infrared spectra) or system polarizability tensor (for Raman spectra). The system dipole moments and polarizability tensors were calculated along the MD trajectories using the many-body MB-μ and MB-α

representations introduced in Ref. 73.

The vibrational spectra were calculated within the time-correlation function (TCF) formalism that relies on the following expressions. The IR activity is calculated as[73,82]

$$I_{\mathrm{IR}}(\omega) = \left[\frac{2\omega}{3V\hbar c\epsilon_0}\right] \tanh\left(\beta\hbar\omega\right) \int_{-\infty}^{\infty} dt\, e^{-i\omega t} \langle \boldsymbol{\mu}(0)\boldsymbol{\mu}(t)\rangle \tag{1}$$

with V the system volume, c the speed of light, ϵ_0 the permittivity of free space, and $\beta = (kT)^{-1}$, with k the Boltzmann constant. The unpolarized Raman activity is calculated as[73,82–84]

$$I_{\mathrm{Raman}}(\omega) = \frac{2\omega}{(\omega_I - \omega)^4} \tanh\left(\beta\hbar\omega\right) \int_{-\infty}^{\infty} dt\, e^{-i\omega t} \langle \boldsymbol{\alpha}(0)\boldsymbol{\alpha}(t)\rangle \tag{2}$$

and can be decomposed into isotropic

$$I_{\mathrm{iso}}(\omega) = \frac{2\omega}{(\omega_I - \omega)^4} \tanh\left(\beta\hbar\omega\right) \int_{-\infty}^{\infty} dt\, e^{-i\omega t} \langle \bar{\alpha}(0)\bar{\alpha}(t)\rangle \tag{3}$$

and depolarized

$$I_{\mathrm{dep}}(\omega) = \frac{2\omega}{(\omega_I - \omega)^4} \tanh\left(\beta\hbar\omega\right) \int_{-\infty}^{\infty} dt\, e^{-i\omega t} \langle \mathrm{Tr}\left[\boldsymbol{\beta}(0)\boldsymbol{\beta}(\mathrm{t})\right]\rangle \tag{4}$$

contributions. Here, ω_I is the frequency of the incident laser (20,500 cm^{-1}, corresponding to a wavelength of 488 nm), $\bar{\alpha} = (\alpha_{xx} + \alpha_{yy} + \alpha_{zz})/3$ the isotropic component and $\boldsymbol{\beta}$ the anisotropic component, respectively, of the polarizbaility tensor $\boldsymbol{\alpha} = \bar{\alpha}\boldsymbol{I} + \boldsymbol{\beta}$, with $\boldsymbol{I}$ the unit tensor.

The normal mode displacements and frequencies were obtained from the diagonalization of the Hessian matrix of the simulation box in periodic boundary conditions. For this analysis, frames were extracted from classical MD trajectories propagated at 10 K. Within the normal mode approximation, the IR and Raman spectra were then calculated from

numerical derivatives of the dipole moment and polarizability along each normal mode, respectively, as approximations to the transition dipole moment and polarizability tensor. Within the normal mode approximation, the transition dipole moment is expressed as

$$\left|\frac{\partial \boldsymbol{\mu}}{\partial \boldsymbol{q}}\right| \approx \left|\frac{1}{\Delta q}\left(\boldsymbol{\mu}_{\text{init}} - \boldsymbol{\mu}_{\text{disp}}\right)\right| \propto \sqrt{\left(\mu_{x,\text{int}} - \mu_{x,\text{disp}}\right)^2 + \left(\mu_{y,\text{int}} - \mu_{y,\text{disp}}\right)^2 + \left(\mu_{z,\text{int}} - \mu_{z,\text{disp}}\right)^2}. \tag{5}$$

The transition isotropic polarizability tensor is expressed as

$$\left|\frac{\partial \bar{\alpha}}{\partial \boldsymbol{q}}\right| \approx \left|\frac{1}{\Delta q}\left(\bar{\alpha}_{\text{init}} - \bar{\alpha}_{\text{disp}}\right)\right| \tag{6}$$

and the transition depolarized polarizability tensor is expressed as

$$\left|\frac{\partial \text{Tr}\left[\boldsymbol{\beta}\cdot\boldsymbol{\beta}\right]}{\partial q}\right| \approx \left|\frac{1}{\Delta q}\left(\text{Tr}\left[\boldsymbol{\beta}_{\text{init}}\cdot\boldsymbol{\beta}_{\text{init}}\right] - \text{Tr}\left[\boldsymbol{\beta}_{\text{disp}}\cdot\boldsymbol{\beta}_{\text{disp}}\right]\right)\right|. \tag{7}$$

These electrostatic transitions for each mode were then broadened with Gaussians with standard deviations of 10 cm^{-1}, providing approximate IR and Raman spectra.

In the same vein as Ref. 43 and following from Ref. 52, we define here a symmetric and antisymmetric index,

$$S_k = \frac{1}{N}\sum_{i=1}^{N}\left|\left(\Delta||\text{OH}_1^{(i)}|| + \Delta||\text{OH}_2^{(i)}||\right)\right| \tag{8}$$

$$A_k = \frac{1}{N}\sum_{i=1}^{N}\left|\left(\Delta||\text{OH}_1^{(i)}|| - \Delta||\text{OH}_2^{(i)}||\right)\right|. \tag{9}$$

Here $||\text{OH}_j^{(i)}||$ is the jth OH bond length ($j = 1, 2$) of the ith water molecule and $\Delta||\text{OH}_1^{(i)}|| = ||\text{OH}_1^{(i)}||_{\text{eq}} - ||\text{OH}_1^{(i)}||_{\Delta q}$ is the change in OH bond length between the optimized equilibrium configuration and the normal mode configuration. For a mode where all molecules undergo symmetric stretching of equal displacement d_{max}, $S_k \to 2d_{\text{max}}$ and $A_k \to 0$. For simplicity, a single normalized stretching index F_k^S will be defined as the fraction of symmetric stretching

to the total symmetric and antisymmetric stretching,

$$F_k^S = \frac{S_k}{S_k + A_k}. \tag{10}$$

This index ranges from 0 to 1, where 1 should be interpreted as the entirety of the OH stretching is symmetric and a value of 0 indicates the OH stretching is entirely antisymmetric. Of course, a complimentary index for the antisymmetric stretching could also be defined as $F_k^A = 1 - F_k^S$.

In addition to the symmetry index, a localization index m_k is defined as

$$m_k = \frac{\mathrm{Max}\,(D_i)}{\sum_{i=1}^{N} D_i} \tag{11}$$

where $D_i = \sum_{j=x,y,z} |d_j^{(i)}|^2$ and $d_j^{(i)}$ is the displacement of the oxygen atom of the ith water molecule along the jth Cartesian axis in the kth normal mode. For a normal mode localized on a single water molecule, $m_k \to 1$, while $m_k \to 1/N$ for a normal mode equally delocalized over all water molecules.

Results and Discussion

Structure

The proton ordered phases of ice form at different pressure regimes, with ice XI found at the lowest pressure conditions (below ∼0.25 GPa), ices II, IX, and XIII existing between ∼0.25 and 1 GPa, and ices VIII, XIV, and XV being found above 1 GPa.[11,31] Their densities also increase in unison with the pressure. Oxygen-oxygen radial distribution functions (RDFs) of ice I_h and all ordered ice phases are presented in Figure 1, calculated from 100 ps NVT simulations at 100 K. Ice I_h has a characteristic hexagonal structure with water molecules hydrogen bonded to one another and arranged in six-membered rings.[11] The basic structure

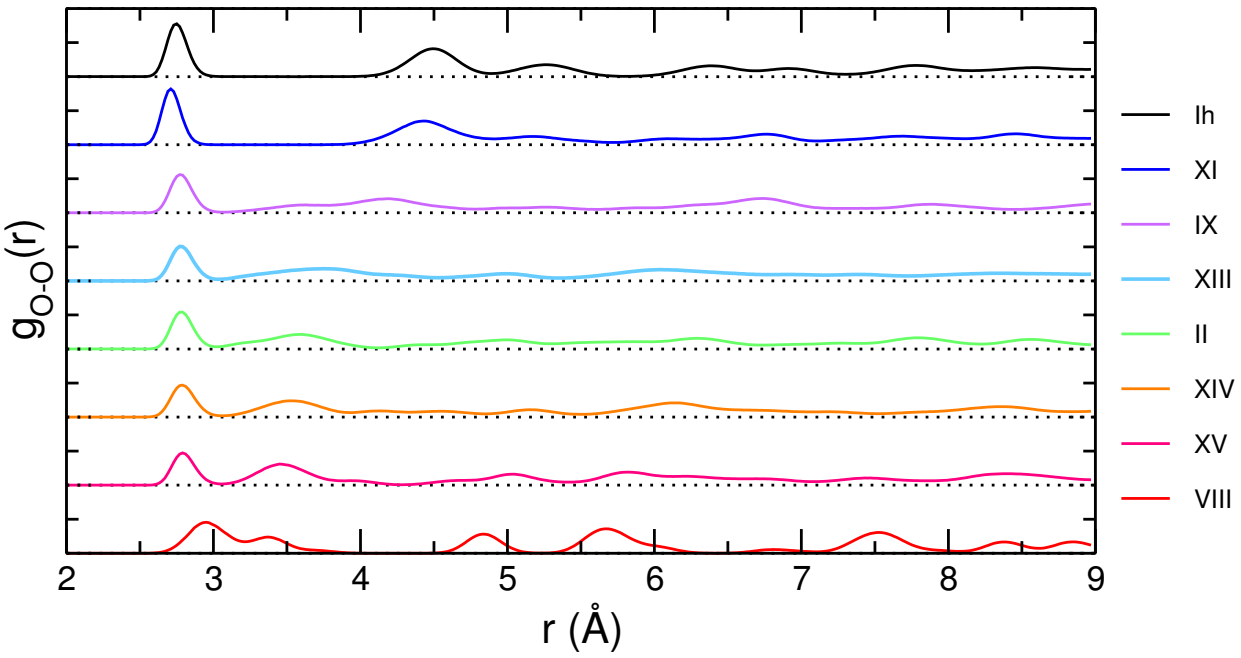

Figure 1: O-O radial distribution functions of ice phases calculated from 100 ps NVT trajectories at 100 K.

is a series of alternating layers composed of chair-form and boat-form hexamers. For comparison, cubic ice (I_c) shares the same local hexagonal oxygen configuration as ice I_h, but consists of entirely chair-form hexamers resulting in a different packing geometry. However, due to sharing the same local structure (their RDFs are identical up to ∼4 Å) and having long-range proton disorder, ice I_h and I_c display essentially identical infrared and Raman spectra.[11,16,18] While ice XI is the ordered form of ice I_h and therefore displays the same underlying hexagonal oxygen configuration, its first two peaks in the O-O RDFs are located at shorter radii than that of ice I_h.

The lattice configuration of ice II is comprised of two hydrogen bonded hexamers, one chair-form and the other nearly flat. These hexamers form parallel columns along the *c*-axis which are spanned by eight- and ten-membered rings.[8,55] It is the only ice with no known disordered counterpart. Ice IX is a metastable phase and the ordered form of ice III, with an oxygen lattice structure containing five-membered rings joined together by four-membered rings.[85] Ice II and ice XIII also show similar RDFs, despite not sharing an underlying oxy-

gen configuration directly, with a similar first nearest neighbor position (2.787 vs. 2.785 Å, respectively), as well as a more uniform structure at farther distances. The structures of ices II, IX, and XIII are closely linked, however. Rapid cooling of ice III yields ice IX, as expected, though slower cooling results in ice II.[22,85] However, ice II transforms only to the disordered form of ice XIII, ice V upon heating.[55] Furthermore, both ice II and ice XIII display unique distortions to their local tetrahedral hydrogen bonded networks with the root mean squared deviation from the ideal tetrahedral bond angle of ice II and ice XIII being 16.8°[36] and 18.5°,[35,86] respectively. This similarity in distortion angles suggests that both ice II and ice XIII experience comparable local hydrogen bonding environments despite having different long range structures.

The remaining RDFs belong to the high pressure ices VIII, XIV, and XV, with densities also correspondingly higher.[11,64] Ice VIII and ice XV achieve their high densities through their unique interlocking but non-interconnected lattices. Ice VIII is composed of interlaced I_c lattices,[38] while ice XV can be thought of as consisting of interlocking hexamer units sharing the "cage-like" gas phase water cluster.[87] Ice XIV has the highest density of ices not formed by interlocking lattices.[11] Its structure (along with its proton disordered counterpart, ice XII) is unique among the crystalline ices, consisting of a double-helix motif resulting in seven-membered or larger rings.[88,89] These three high pressure phases, particularly ice VIII, have counter-intuitively larger radii for their first nearest-neighbors than the lower pressure phases. However, the distances to the second nearest-neighbor oxygens are less than in other phases, resulting in overall denser structures.

Vibrational spectra

Vibrational spectroscopy has long been a useful tool to investigate the structure of water and ice. In particular, the OH stretching region, extending from roughly 3000 to 4000 cm^{-1}, provides detailed, though at times difficult to interpret, information about the hydrogen bonding environment, as the stretching modes are direct probes of the hydrogen bond strength in

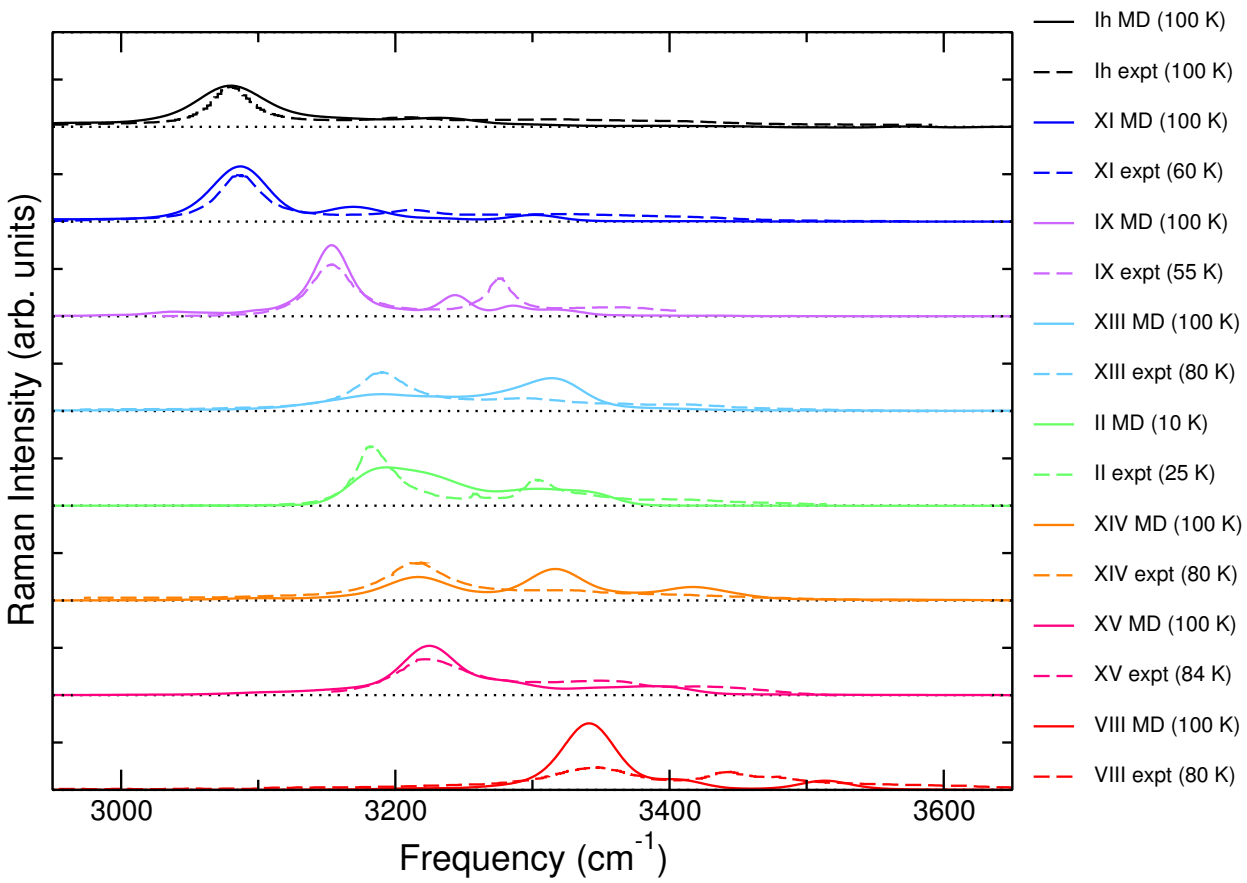

Figure 2: Unpolarized Raman. Experimental data for ice I_h,[90] XI,[90] IX,[20] XIII,[26] II,[20] XIV,[27] XV,[91] and VIII[28] extracted from the indicated studies. The experimental ice XIII and XIV spectra were measured for systems with 9.0 mol% HOD in H_2O. MB-MD spectra calculated from classical MD simulations have been redshifted for comparison with experimental spectra.

aqueous systems. As Raman spectroscopy is generally experimentally better suited to probing the ordered ice phases due to requiring lower powered lasers and the higher degree of scattering created,[55] Raman spectroscopy is a more common experimental technique than infrared spectroscopy. As in Ref. 52 which showed that MB-pol accurately captures the spectral features of ice I_h when compared to experiment, Figure 2 compares unpolarized Raman spectra calculated with classical MB-MD to experimental Raman spectra measured at similar temperatures extracted from various studies.[20,20,26–28,90,91]

In general, the MB-pol/MB-α spectra show excellent agreement with the experimental results. Note that the MB-MD spectra have been redshifted to align the most intense peaks

to account for the lack of nuclear quantum effects in the classical dynamics. This redshift is only an approximate and ad hoc method and, for some ices such as ice IX, leads to poor alignment for the other features. Overall, Ice VIII displays the poorest agreement, mainly in relative peak intensity of the two main features. While the location of the two major peaks are shifted relative to experiment, MB-MD does capture the correct number of features. Perfectly matching experimental and simulation conditions is also difficult, and ice VIII has been shown to be strongly influenced by pressure and temperature.[28,92] It should also be noted that MB-pol performs less well for ice VIII when comparing the lattice energies of the ordered ice phases with experimental measurements,[53] largely due to neglecting the lattice zero point energy. As the simulations performed in this study were classical and therefore neglected nuclear quantum effects such as zero point energy, of particular importance for high density ices such as ice VIII, this may also explain the poorer agreement of the relative peak intensities observed in Figure 2 for ice VIII between experimental data[28] and MB-MD simulations.

As discussed in Ref. 52, the lack of nuclear quantum effects can lead to narrower individual peaks and smaller overall spectral ranges as a result of the steeper potential energy surface experienced by the system. The majority of the MB-MD spectra displayed in Figure 2, however, appear to show minimal narrowing of spectral peaks when compared with experimental spectra. This is likely due to the low temperatures the experiments and simulations were performed at, resulting in less thermal broadening effects overall that need to be captured by the classical simulations. Another possible explanation is the proton ordering yielding less inhomogeneous broadening, though this was shown to not be a contributing factor in ice XI.[90]

The general agreement of MB-MD with experimental Raman spectra, as well as ice I_h being shown previously to match the experimental IR spectrum,[52] suggests MB-MD can satisfactorily capture the important spectral features of the various ordered ice phases. To better understand the molecular level details of the spectra, normal mode (NM) calculations

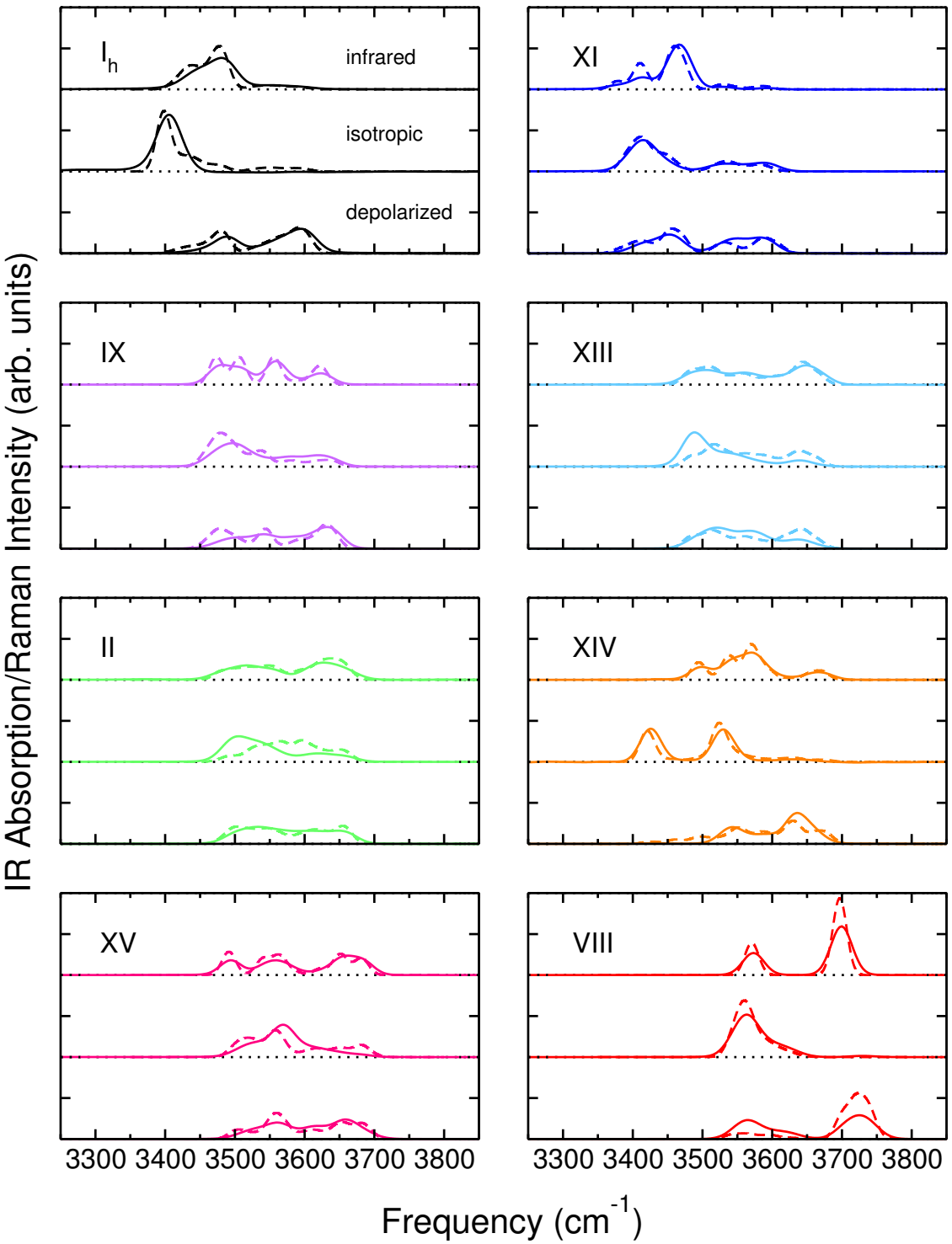

Figure 3: Shown for each ice, from top to bottom, are the MB-MD (solid) and normal mode (dashed) derived infrared, isotropic Raman, and depolarized Raman spectra.

are employed. As explored in Ref. 52, the obtained frequencies can be combined with approximations to the transition dipole moments and transition isotropic and anisotropic polarizability tensors. Together, these yield effective IR and Raman spectra after artificial broadening with Gaussian functions. The agreement between the MB-MD spectra and NM spectra provides a measure of the validity of the NM treatment, allowing for further analysis to provide physically meaningful interpretations. More details on this process are provided in the Supporting Information as well as in Ref. 52.

Normal mode calculations have been previously performed on primitive cells of some ordered ice phases containing 2^{66} or 4 molecules.[15,67] While these phonon mode studies allow for precise assigning of peaks in terms of molecular motions, the effects of delocalization can not be properly investigated with single unit cells. An earlier study on ice I_h using a model Hamiltonian also introduced a similar symmetry index to Eq. 10, referred to therein as the fractional symmetric character.[43] Both Refs. 43 and 52 claim the interpretation of the ice I_h spectrum in terms of molecular vibrational modes is not appropriate. Instead of the spectral peaks being assignable to well-defined symmetric and antisymmetric stretch modes, at best the peaks generally have only a majority of one stretch motion in a given region, while other regions contain a mixture of symmetric and antisymmetric stretching. The method of analyzing the normal mode calculations of ice I_h described in Ref. 52 is here applied to the ordered ice phases. Figure 3 shows the calculated infrared, isotropic Raman, and depolarized Raman spectra from both MB-MD and NM analysis. For every ice phase, the spectra display excellent agreement between the MB-MD and NM spectra, allowing for some small discrepancies due to the artificial line broadening through Gaussian functions. Key features to note are the large variances in frequency ranges spanned by the different phases, with ice XI/I_h being the most redshifted spectra, and ice VIII the most blueshifted. Note that, unlike Figure 2, the spectra in Figure 3 have not been redshifted to account for the lack of nuclear quantum effects.

It must be noted that the isotropic Raman spectra shown in Figure 3 for ices XI, IX, XV,

and VIII were modified by removing single modes with artificially strong isotropic peaks. These strong intensities are a result of the highly symmetric nature of the ordered phases and the resulting normal mode approach overestimates the isotropic signal produced from some modes with a high degree of symmetric stretching, which the isotropic Raman signal is sensitive to. These single large intensity modes lead to poor agreement with the MB-MD spectra for the ice phases where they appear. Comparing ice I_h and XI, the disorder of ice I_h dampens the effect of the concerted stretching motion seen in the ordered ice XI. The spectra before removing the artificially large isotropic modes are shown in the Supporting Information.

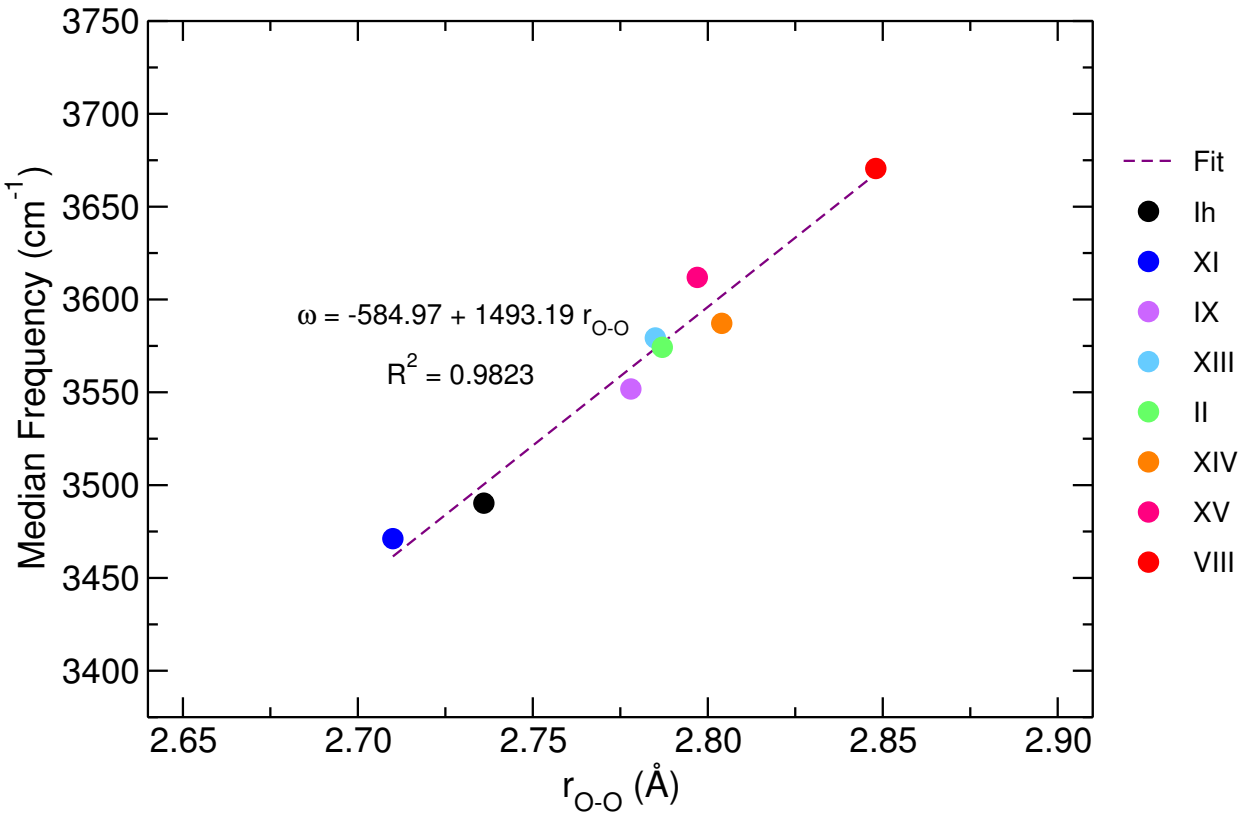

Figure 4: Correlation between the peak position of the first nearest neighbors in the O-O RDF at 10 K and the median NM frequency for each ice phase. Also shown is the linear fit obtained from the data.

As discussed previously, ices VIII, XIV, and XV are high pressure and high density ices, though their first oxygen-oxygen nearest neighbors are in fact located at farther distances

than the lower pressure ices, as shown in the O-O RDFs of Figure 1. This is explained by the fact that their second nearest-neighbors are located at much closer distances than the lower density ices, yielding an overall higher density. Figure 4 shows the correlation between the position of the first nearest-neighbor peak of the O-O RDFs at 10 K (RDFs at 10 K are provided in the Supporting Information) and the median frequency obtained from the normal mode calculations for the various ice phases. Also shown is the linear fit to the data. The ice phases follow a general trend of larger spacing between neighboring water molecules leading to a higher frequency OH stretching region. This suggests the first coordination shell predominantly affects the frequency shift in the OH stretching region, with the second nearest neighbors having little influence. This follows from the stronger hydrogen bond formed as the water molecules are forced closer together. Also apparent is that of the ordered ice phases, ices XI and VIII are outliers, found at either extreme of the observed trend, with the remaining ices clustered in a more central group. The trend can be understood as, if taken to the extreme case of large r_{O-O}, approaching a gas phase water molecule with neighboring water molecules at large distances. The median stretching frequency would approach that of a gas phase water molecule.

Indexes

The normal mode analysis also allows for molecular level detail of the ice spectra with each mode examined individually. This is accomplished here through the categorization of each mode through indexes, namely the degree of symmetric/antisymmetric stretching present in a mode and the amount of displacement caused by the stretching motion as a measure of localization.[52] Figure 5 shows the normalized symmetric stretching parameter described in Eq. 10. For each mode, the index ranges between 0 and 1, with 0 describing a system where all stretches are antisymmetric, 1 where all stretches are symmetric, and transitional values referring to a mixture of both symmetric and antisymmetric stretching. There is a clear trend of lower frequencies having mainly symmetric stretching character, logically

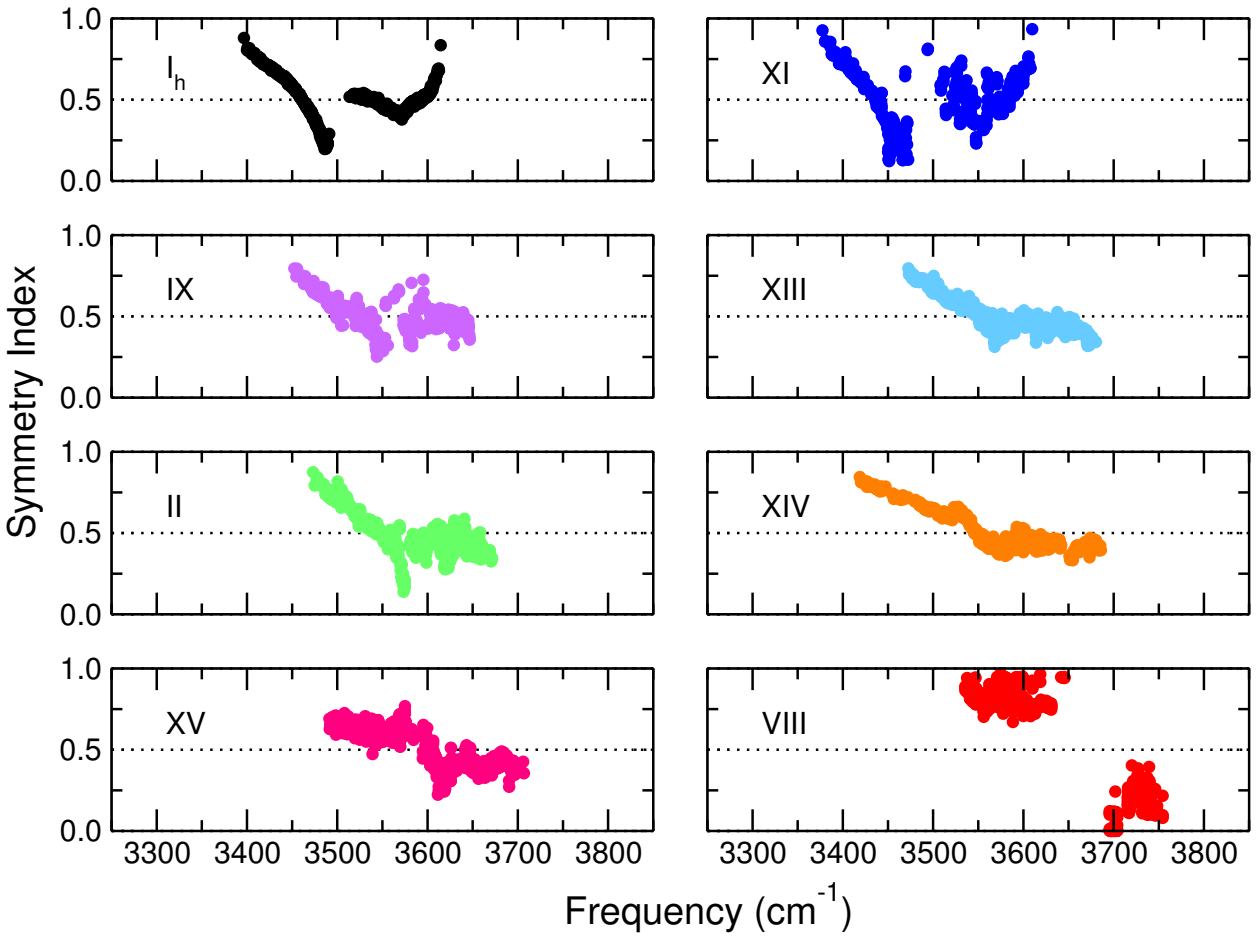

Figure 5: Symmetry index calculated for each mode in each ice ordered phase and ice I_h. Shown is the ratio of symmetric stretching to total stretching character of a given mode, F_k^S, as described in Eq. 10.

corresponding to regions where isotropic Raman signals tend to be strongest. Shifting to higher frequency yields a mixture of both symmetric and antisymmetric stretching for most ices, with the ratio eventually leveling off and remaining roughly equally divided between symmetric and antisymmetric.

Ice I_h/XI deviates somewhat at their highest frequency values, with regions of high symmetry appearing again around 3600-3650 cm^{-1}. The relations between the spectra and indexes for ice I_h were discussed in Ref. 52, and ice XI follows similar trends. They both display weak IR signals in this region, whereas the other ice phases besides ice VIII have generally retain roughly the same IR intensity over their entire range. Experimental spectra[29,90]

show little to no difference in peak width between ice I_h and XI for both IR and Raman spectra in the OH stretching region. While both this study and a previous computational study[51] of ice I_h and XI show a moderate decrease in peak width due to proton ordering in the OH stretching region, it is minimal compared to what would be expected for a hydrogen ordered ice. This suggests delocalized coupling between modes, not proton disorder, is the main cause of the broad linewidth observed in both ice I_h and XI.[50,52,90]

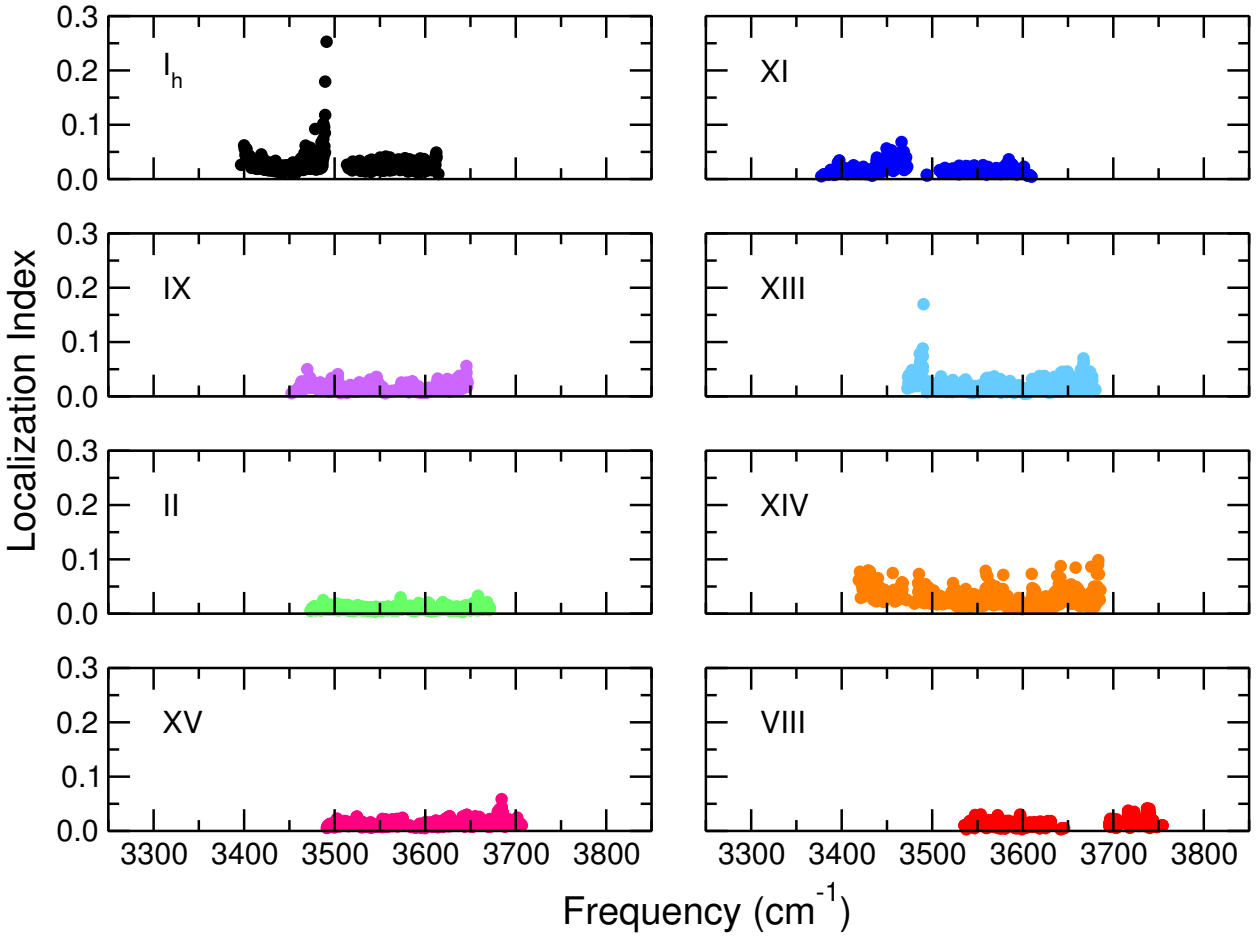

Figure 6: Localization index, as described in Eq. 11, calculated for each mode in each ice ordered phase and ice I_h.

Figure 6 shows the localization index described in Eq. 11 calculated for each normal mode of each ice phase. This index quantifies the number of molecules participating in a vibrational mode by totaling their displacements from the equilibrium position in each cartesian direction. In general, the ordered phases are overall highly delocalized, and more

delocalized than the disordered ice I_h, though only in narrow regions does ice I_h possess highly localized modes. For a direct comparison, ice I_h has one highly localized region near 3490 cm^{-1}, in the region of largest IR activity.[52] This region contains the largest value of m_k across ice I_h and all the disordered phases of 0.25, which can be interpreted as $\sim$4 water molecules participating in the mode. In the corresponding region of strongest IR activity for ice XI around 3460 cm^{-1}, the largest value of m_k is only 0.08, which can be interpreted as $\sim$12 molecules participating in the mode. Elsewhere, however, ice XI shows a similar degree of localization as ice I_h. As discussed, Ref. 90 measured the spectra of ice I_h and XI to have similar lineshapes, both in terms of peak position and width, despite the ordered ice XI theoretically having less inhomogeneous broadening and, therefore, narrower spectral peaks. They proposed this to be due to delocalization and intermolecular coupling being strong in both systems. Other than the small region near 3490 cm^{-1}, the localization index values in Figure 6 are similar for ice I_h and ice XI, supporting the notion that both have mostly delocalized modes.

Visualizations of selected modes are provided in Figure 7. Blue spheres represent water molecules with predominantly symmetric stretching ($F_k^S > 0.5$) and red spheres represent water molecules with $F_k^S < 0.5$, or antisymmetric stretching. The opacity of a sphere is proportional to the localization index normalized to the largest value of m_k across all ice phases, which as mentioned is 0.25 in the strong IR region of ice I_h. Shown in the left column of Figure 7 are the most symmetric modes in ice I_h, ice XI, and ice VIII. These all correspond to the regions with the most intense peak in the isotropic Raman spectra in Figure 3. The right column of Figure 7 showcase modes with the most intense IR signal.

The visualizations allow for comparison between the different ice phases. The strongest isotropic modes of ices I_h and XI, which are also the most symmetric modes, are not equally delocalized. The 3396 cm^{-1} ice I_h mode has a darker region on the right side of the lattice, signifying a slightly more localized mode than the 3388 cm^{-1} mode of ice XI. This can be attributed to the disordered ice I_h lattice configuration, where variation in local environments

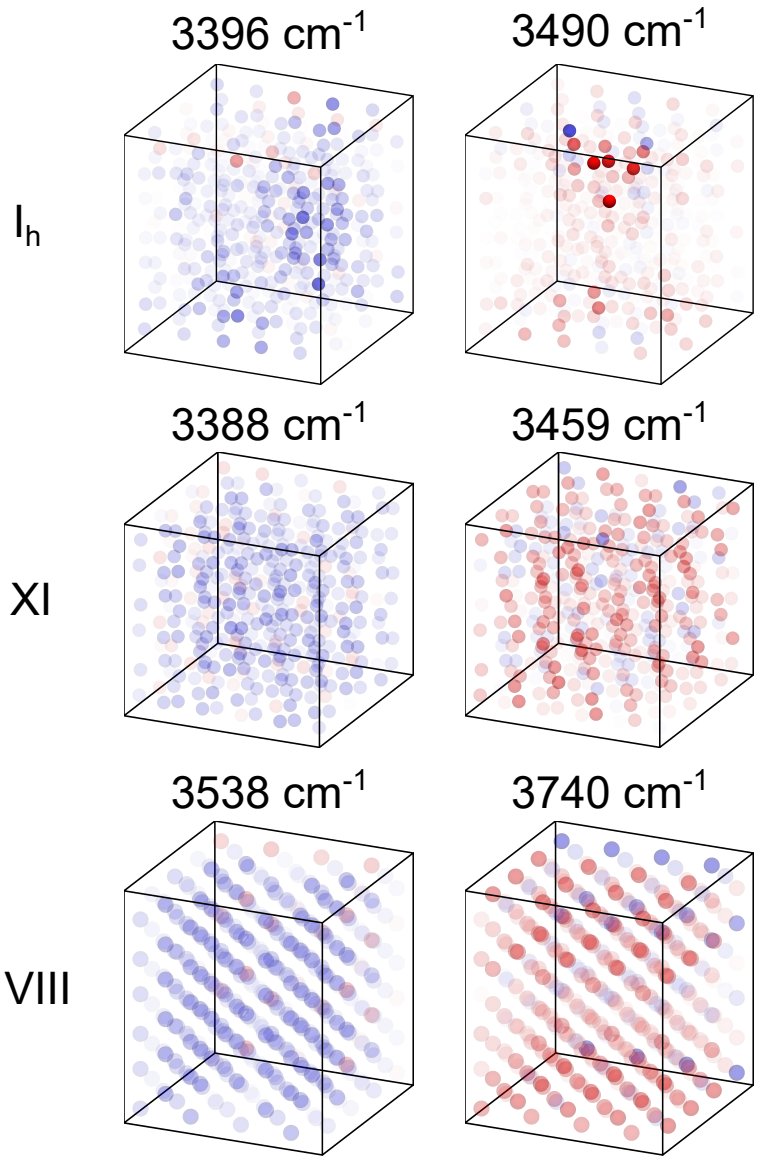

Figure 7: Visualizations of selected normal modes for ices I_h, XI, and VIII. Blue spheres represent water molecules with predominantly symmetric stretching ($F_k^S > 0.5$) and red spheres represent water molecules with $F_k^S < 0.5$, or antisymmetric stretching. The opacity of a sphere is proportional to the localization index normalized to the largest value of m_k across all ice phases. Left column: the mode for each ice with the largest isotropic signal. Right column: the mode for each ice with the largest infrared signal.

due to proton disorder limits the extent of delocalization of the mode across the lattice. The strong infrared modes in the right column of Figure 7 display much wider discrepancies in localization, with a small localized region of motion in ice I_h clearly visible. In contrast, ice XI, being an ordered phase, possesses a more periodic lattice allowing for greater delocalization

of vibrational modes and intermolecular coupling of modes across the lattice. However, for most modes, this increase in delocalization is negligible, only affecting the localized modes with strong infrared intensity.

In general, a straightforward assignment of the infrared and Raman spectral peaks for the ordered ice phases based on well-defined regions of symmetry and antisymmetry proves to be impossible. The regions can rarely be described in terms of only symmetric or antisymmetric stretching due to the delocalization and intermolecular coupling of vibrational modes.[50,90] The one exception to this is ice VIII, which possesses two distinct regions with predominantly symmetric (3500-3650 cm^{-1}) and antisymmetric (3700-3750 cm^{-1}) F_k^S values, examples of which are depicted in Figure 7. Both the symmetric 3538 cm^{-1} mode and antisymmetric 3740 cm^{-1} mode are almost evenly delocalized across the lattice, a result of the unique lattice configuration of ice VIII. This suggests that ice VIII alone can be reasonably described by the molecular normal modes of water. In other words, the two main spectral features, at low and high frequency, seen in the Raman and infrared spectra of Figures 2 and 3 can be confidently assigned to be symmetric stretching and antisymmetric stretching modes, respectively. This is in contrast to ice I_h, as discussed in Ref. 52, as well as the other ordered ice phases. The large spacing between neighboring oxygens, as demonstrated in Figures 1 and 4, may explain this, as ice VIII was also an outlier in this regard. The water molecules in ice VIII, despite being denser overall, have more space between their closest neighbors.

Conclusions

Simulated IR and Raman spectra were calculated for the proton ordered ice phases through many-body molecular dynamics combined with many-body electrostatic surfaces. MB-MD Raman spectra had good agreement when compared to experimental Raman spectra in Figure 2. With these results providing credence to the use of classical mechanics with MB-pol for capturing ice spectral features, in addition to previous studies showing MB-

pol accurately capturing the lattice energies of the ordered ice phases[53] and the classical vibrational spectra of ice I_h,[52] normal mode analyses were then carried out for each ordered ice phase to gain deeper insight into the origin of the observed MB-MD spectral features. From the normal mode calculations, symmetry and localization indexes were calculated for each vibrational mode, a continuation of the method detailed in Ref. 52. These provide molecular level explanations for the vibrational spectra of the ordered ice phases and their underlying structural relationships.

There is a clear trend between the closest oxygen-oxygen distance for each ice phase and the median frequency as calculated through normal mode analysis, shown in Figure 4, with larger O-O distances yielding higher median frequencies. As the water molecules in the ices have more space in their immediate surroundings, the hydrogen bonding is weakened, leading to stronger OH bonds and larger stretching frequencies. The ice phases also can be considered occupying three distinct groups in the correlation plot, with a main group comprised of ices II, IX, XIII, XIV, and XV, and two remaining groups composed of single ices, each being outliers on either extreme of the main group. The symmetry and localization indexes of Figure 5 support previous work on ice I_h and XI that their similar spectral signatures are due to high delocalization of modes in both ices. While most of the ices display a mixture of symmetric and antisymmetric stretching across all modes, preventing assignment of features in terms of the traditional molecular modes of water, ice VIII is unique, having well-defined regions of symmetry and antisymmetry.

This study investigated only the OH stretching region as a probe of the hydrogen bonding networks of the ice phases. However, the low frequency librational region provides valuable information on the lattice structure, and the same normal mode analysis detailed here could well be applied to this and other vibrational regions. Furthermore, this study used only classical molecular dynamics methods with MB-pol. Testing MB-pol with a more robust quantum dynamics method could improve the agreement with experimental spectra, particularly the high density ice VIII.

Supporting Information

Included in the Supporting Information are radial distribution functions calculated at 10 K and isotropic Raman spectra that include the unrealistically intense low frequency mode for ices XI, IX, XV, and VIII.

Acknowledgements

This research was supported by the National Science Foundation through grant no. CHE-1453204 and used resources of the Extreme Science and Engineering Discovery Environment (XSEDE),[93] which is supported by the National Science Foundation through grant no. ACI-1053575, under allocation TG-CHE110009 on Comet at the San Diego Supercomputer Center and Stampede2 at the Texas Advanced Computing Center.

References

(1) Bartels-Rausch, T.; Bergeron, V.; Cartwright, J. H. E.; Escribano, R.; Finney, J. L.; Grothe, H.; Gutiérrez, P. J.; Haapala, J.; Kuhs, W. F.; Pettersson, J. B. C. et al. Ice Structures, Patterns, and Processes: A View Across the Icefields. *Rev. Mod. Phys.* **2012**, *84*, 885–944.

(2) Fukuzawa, H.; Mae, S.; Ikeda, S.; Watanabe, O. Proton Ordering in Antarctic Ice Observed by Raman and Neutron Scattering. *Chem. Phys. Lett.* **1998**, *294*, 554–558.

(3) Fortes, A. D.; Wood, I. G.; Grigoriev, D.; Alfredsson, M.; Kipfstuhl, S.; Knight, K. S.; Smith, R. I. No Evidence for Large-Scale Proton Ordering in Antarctic Ice from Powder Neutron Diffraction. *J. Chem. Phys.* **2004**, *120*, 11376.

(4) Kennett, J. P.; Cannariato, K. G.; Hendy, I. L.; Behl, R. J. *Methane Hydrates in Quaternary Climate Change: The Clathrate Gun Hypothesis*; American Geophysical Union: Washington, DC, USA, 2003.

(5) Murray, B. J.; Knopf, D. A.; Bertram, A. K. The Formation of Cubic Ice Under Conditions Relevant to Earth's Atmosphere. *Nature* **2005**, *434*, 202–205.

(6) Vance, S.; Bouffard, M.; Choukroun, M.; Sotin, C. Ganymede's Internal Structure Including Thermodynamics of Magnesium Sulfate Oceans in Contact with Ice. *Planet. Space Sci.* **2014**, *96*, 62–70.

(7) Filacchione, G.; De Sanctis, M. C.; Capaccioni, F.; Raponi, A.; Tosi, F.; Ciarniello, M.; Cerroni, P.; Piccioni, G.; Capria, M. T.; Palomba, E. et al. Exposed Water Ice on the Nucleus of Comet 67P/Churyumov–Gerasimenko. *Nature* **2016**, *529*, 368–372.

(8) Tammann, G. Ueber die Grenzen des festen Zustandes IV. *Annalen der Physik* **1900**, *307*, 1–31.

(9) Bridgman, P. W. Water, in the Liquid and Five Solid Forms, Under Pressure. *Proc. Am. Acad. Arts Sci.* **1912**, *47*, 441–558.

(10) Bernal, J. D.; Fowler, R. H. A Theory of Water and Ionic Solution, with Particular Reference to Hydrogen and Hydroxyl Ions. *J. Chem. Phys.* **1933**, *1*, 515–548.

(11) Salzmann, C. G.; Radaelli, P. G.; Slater, B.; Finney, J. L. The Polymorphism of Ice: Five Unresoled Questions. *Phys. Chem. Chem. Phys.* **2011**, *13*, 18468–18480.

(12) Falenty, A.; Hansen, T. C.; Kuhs, W. F. Formation and Properties of Ice XVI Obtained by Emptying a Type sII Clathrate Hydrate. *Nature* **2014**, *516*, 231–233.

(13) del Rosso, L.; Celli, M.; Ulivi, L. New Porous Water Ice Metastable at Atmospheric Pressure Obtained by Emptying a Hydrogen-Filled Ice. *Nat. Commun.* **2016**, *7*, 13394.

(14) Petrenko, V. F.; Whitworth, R. W. *Physics of Ice*; Oxford University Press, Oxford, 1999.

(15) Zhang, P.; Wang, Z.; Lu, Y.-B.; Ding, Z.-W. The Normal Modes of Lattice Vibrations of Ice XI. *Sci. Rep.* **2016**, *6*, 29273.

(16) Bertie, J. E.; Whalley, E. Infrared Spectra of Ices Ih and Ic in the Range 4000 to 350 cm^{-1}. *J. Chem. Phys.* **1964**, *40*, 1637.

(17) Bertie, J. E.; Whalley, E. Infrared Spectra of Ices II, III, and V in the Range 4000 to 350 cm^{-1}. *J. Chem. Phys.* **1964**, *40*, 1646.

(18) Taylor, M. J.; Whalley, E. Raman Spectra of Ices Ih, Ic, II, III, and V. *J. Chem. Phys.* **1964**, *40*, 1660.

(19) Bertie, J. E.; Bates, F. E. Mid-Infrared Spectra of Deuterated Ices at 10° K and Interpretation of the OD Stretching Bands of Ices II and IX. *J. Chem. Phys.* **1977**, *67*, 1511.

(20) Bertie, J. E.; Francis, B. F. Raman Spectra of the O-H and O-D Stretching Vibrations of Ices II and IX to 25° K at Atmospheric Pressure. *J. Chem. Phys.* **1980**, *72*, 2213.

(21) Wong, P. T. T.; Whalley, E. Raman Spectrum of Ice VIII. *J. Chem. Phys.* **1976**, *64*, 2359.

(22) Šukarova, B.; Sherman, W. F.; Wilkinson, G. R. Raman Spectra Of The High Pressure Phases of Ice In Their Region Of Stability. *J. Mol. Struct.* **1982**, *79*, 289–292.

(23) Mincĕva-Šukarova, B.; Sherman, W. F.; Wilkinson, G. R. The Raman Spectra of Ice (I_h, II, III, V, VI, and IX) as Functions of Pressure and Temperature. *J. Phys. C: Solid State Phys.* **1984**, *17*, 5833–5850.

(24) Song, M.; Yamawaki, H.; Fujihisa, H.; Sakashita, M.; Aoki, K. Infrared Investigation on Ice VIII and the Phase Diagram of Dense Ices. *Phys. Rev. B* **2003**, *68*, 014106.

(25) Pruzan, P.; Chervin, J. C.; Wolanin, E.; Canny, B.; Gauthier, M.; Hanfland, M. Phase Diagram of Ice in the VII-VIII-X Domain. Vibrational and Structural Data for Strongly Compressed Ice VIII. *J. Raman Spectrosc.* **2003**, *34*, 591–610.

(26) Salzmann, C. G.; Hallbrucker, A.; Finney, J. L.; Mayer, E. Raman Spectroscopic Study of Hydrogen Ordered Ice XIII and of its Reversible Phase Transition to Disordered Ice V. *Phys. Chem. Chem. Phys.* **2006**, *8*, 3088–3093.

(27) Salzmann, C. G.; Hallbrucker, A.; Finney, J. L.; Mayer, E. Raman Spectroscopic Features of Hydrogen-Ordering in Ice XII. *Chem. Phys. Lett.* **2006**, *429*, 469–473.

(28) Yoshimura, Y.; Stewart, S. T.; Somayazula, M.; Mao, H.; Hemley, R. J. High-Pressure X-Ray Diffraction and Raman Spectroscopy of Ice VIII. *J. Chem. Phys.* **2006**, *124*, 024502.

(29) Arakawa, M.; Kagi, H.; Fukazawa, H. Laboratory Measurements of Infrared Absorption Spectra of Hydrogen-ordered Ice: A Step to the Exploration of Ice XI in Space. *Astrophys. J. Suppl. S.* **2009**, *184*, 361.

(30) Whale, T. F.; Clark, S. J.; Finney, J. L.; Salzmann, C. G. DFT-Assisted Interpretation of the Raman Spectra of Hydrogen-Ordered Ice XV: Raman Spectra of Hydrogen-Ordered Ice XV. *J. Raman Spectrosc.* **2013**, *44*, 290–298.

(31) Wang, Y.; Zhang, H.; Yang, X.; Jiang, S.; Goncharov, A. F. Kinetic Boundaries and Phase Transformations of Ice I at High Pressure. *J. Chem. Phys.* **2018**, *148*, 044508.

(32) Peterson, S. W.; Levy, H. A. A Single-Crystal Neutron Diffraction Study of Heavy Ice. *Acta Cryst.* **1957**, *10*, 70–76.

(33) Kamb, B. Ice II: A Proton-Ordered Form of Ice. *Acta Cryst.* **1964**, *17*, 1437–1449.

(34) Kamb, B. Structure of Ice VI. *Science* **1965**, *150*, 205–209.

(35) Kamb, B.; Prakash, A.; Knobler, C. Structure of Ice V. *Acta Cryst.* **1967**, *22*, 706–715.

(36) Kamb, B.; Hamilton, W. C.; LaPlaca, S. J.; Prakash, A. Ordered Proton Configuration in Ice II, from Single-Crystal Neutron Diffraction. *J. Chem. Phys.* **1971**, *55*, 1934.

(37) Jorgensen, J. D.; Beyerlein, R. A.; Watanabe, N.; Worlton, T. G. Structure of D_2O Ice VIII from In Situ Powder Neutron Diffraction. *J. Chem. Phys.* **1984**, *81*, 3211.

(38) Kuhs, W. F.; Finney, J. L.; Vettier, C.; Bliss, D. V. Structure and Hydrogen Ordering in Ices VI, VII, and VIII by Neutron Powder Diffraction. *J. Chem. Phys.* **1984**, *81*, 3612.

(39) Jackson, S. M.; Nield, V. M.; Whitworth, R. W.; Oguro, M.; Wilson, C. C. Single-Crystal Neutron Diffraction Studies of the Structure of Ice XI. *J. Phys. Chem. B* **1997**, *101*, 6142–6145.

(40) Shephard, J. J.; Salzmann, C. G. The Complex Kinetics of the Ice VI to Ice XV Hydrogen Ordering phase transition. *Chem. Phys. Lett.* **2015**, *637*, 63–66.

(41) Salzmann, C. G.; Slater, B.; Radaelli, P. G.; Finney, J. L.; Shephard, J. J.; Rosillo-Lopez, M.; Hindley, J. Detailed Crystallographic Analysis of the Ice VI to Ice XV Hydrogen Ordering Phase Transition. *J. Chem. Phys.* **2016**, *145*, 204501.

(42) Bosi, P.; Tubino, R.; Zerbi, G. On the Problem of the Vibrational Spectrum and Structure of Ice Ih: Lattice Dynamical Calculations. *J. Chem. Phys.* **1973**, *59*, 4578.

(43) McGraw, R.; Madden, W. G.; Bergren, M. S.; Rice, S. A.; Sceats, M. G. A Theoretical Study of the OH Stretching Region of the Vibrational Spectrum of Ice Ih. *J. Chem. Phys.* **1978**, *69*, 3483.

(44) Knuts, S.; Ojamäe, L.; Hermansson, K. An Ab Initio Study of the OH Stretching Frequencies in Ice II, Ice VIII, and Ice IX. *J. Chem. Phys.* **1993**, *99*, 2917.

(45) Bernasconi, M.; Silvestrelli, P. L.; Parrinello, M. Ab Initio Infrared Absorption Study of the Hydrogen-Bond Symmetry in Ice. *Phys. Rev. Lett.* **1998**, *81*, 1235–1238.

(46) Putrino, A.; Parrinello, M. Anharmonic Raman Spectra in High-Pressure Ice from Ab Initio Simulations. *Phys. Rev. Lett.* **2002**, *88*, 174601.

(47) Fortes, A. D.; Wood, I. G.; Brodholt, J. P.; Vočadlo, L. Ab Initio Simulation of the Ice II Structure. *J. Chem. Phys.* **2003**, *119*, 4567.

(48) Auer, B. M.; Skinner, J. L. IR and Raman Spectra of Liquid Water: Theory and Interpretation. *J. Chem. Phys.* **2008**, *128*, 224511.

(49) Umemoto, K.; Wentzcovitch, R. M.; de Gironcoli, S.; Baroni, S. Order-Disorder Phase Boundary Between Ice VII and VIII Obtained by First Principles. *Chem. Phys. Lett.* **2010**, *499*, 236–240.

(50) Shi, L.; Gruenbaum, S. M.; Skinner, J. L. Interpretation of IR and Raman Line Shapes for H_2O and D_2O Ice Ih. *J. Phys. Chem. B* **2012**, *117*, 13821–13830.

(51) Liu, Y.; Ojamäe, L. Raman and IR Spectra of Ice Ih and Ice XI with an Assessment of DFT Methods. *J. Phys. Chem. B* **2016**, *120*, 11043–11051.

(52) Moberg, D. R.; Straight, S. C.; Knight, C.; Paesani, F. Molecular Origin of the Vibrational Structure of Ice Ih. *J. Phys. Chem. Lett.* **2017**, *8*, 2579–2583.

(53) Pham, C. H.; Reddy, S. K.; Chen, K.; Knight, C.; Paesani, F. Many-Body Interactions in Ice. *J. Chem. Theory Comput.* **2017**, *13*, 1778–1784.

(54) Whalley, E. A Detailed Assignment of the O-H Stretching Bands of Ice I. *Can. J. Chem.* **1977**, *55*, 3429–3441.

(55) Tran, H.; Cunha, A. V.; Shephard, J. J.; Shalit, A.; Hamm, P.; Jansen, T. L. C.; Salzmann, C. G. 2D IR Spectroscopy of High-Pressure Phases of Ice. *J. Chem. Phys.* **2017**, *147*, 144501.

(56) Perakis, F.; Hamm, P. Two-Dimensional Infrared Spectroscopy of Neat Ice Ih. *Phys. Chem. Chem. Phys.* **2012**, *14*, 6250–6256.

(57) Shi, L.; Skinner, J. L. Proton Disorder in Ice Ih and Inhomogenous Broadening in Two-Dimensional Infrared Spectroscopy. *J. Phys. Chem. B* **2013**, *117*, 15536–15544.

(58) Shi, L.; Skinner, J. L.; Jansen, T. L. C. Two-Dimensional Infrared Spectroscopy of Neat Ice I_h. *Phys. Chem. Chem. Phys.* **2016**, *18*, 3772.

(59) Nanda, K. D.; Beran, G. J. O. What Governs the Proton Ordering in Ice XV? *J. Phys. Chem. Lett.* **2013**, *4*, 3165–3169.

(60) Nakamura, T.; Matsumoto, M.; Yagasaki, T.; Tanaka, H. Thermodynamic Stability of Ice II and its Hydrogen-Disordered Counterpart: Role of Zero-Point Energy. *J. Phys. Chem. B* **2016**, *120*, 1843–1848.

(61) Parkkinen, P.; Riikonen, S.; Halonen, L. Ice XI: Not That Ferroelectric. *J. Phys. Chem. C* **2014**, *118*, 26264–26275.

(62) Fan, X.; Bing, D.; Zhang, J.; Shen, Z.; Kuo, J.-L. Predicting the Hydrogen Bond Ordered Structures of Ice Ih, II, III, VI, and ice VII: DFT Methods with Localized Basis Set. *Comput. Mater. Sci.* **2010**, *49*, S170–S175.

(63) Umemoto, K.; Sugimura, E.; de Gironcoli, S.; Nakajima, Y.; Hirose, K.; Ohishi, Y.; Wentzcovitch, R. M. Nature of the Volume Isotope Effect in Ice. *Phys. Rev. Lett.* **2015**, *115*, 173005.

(64) Umemoto, K.; Wentzcovitch, R. M. First Principles Study of Volume Isotope Effects in Ices VIII and X. *Jpn. J. Appl. Phys.* **2017**, *56*, 05FA03.

(65) Murray, É. D.; Galli, G. Dispersion Interactions and Vibrational Effects in Ice as a Function of Pressure: A First Principles Study. *Phys. Rev. Lett.* **2012**, *108*, 105502.

(66) Yao, S.-K.; Zhang, P.; Zhang, Y.; Lu, Y.-B.; Yang, T.-L.; Sun, B.-G.; Yuan, Z.-Y.; Luo, H.-W. Computing Analysis of Lattice Vibrations of Ice VIII. *RSC Adv.* **2017**, *7*, 31789.

(67) Yuan, Z.-Y.; Zhang, P.; Yao, S.-K.; Lu, Y.-B.; Yang, H.-Z.; Luo, H.-W.; Zhao, Z.-J. Computational Assignments of Lattice Vibrations of Ice Ic. *RSC Adv.* **2017**, *7*, 36801.

(68) Futera, Z.; English, N. J. Pressure Dependence of Structural Properties of Ice VII: An Ab Initio Molecular-Dynamics Study. *J. Chem. Phys.* **2018**, *148*, 204505.

(69) Babin, V.; Leforestier, C.; Paesani, F. Development of a First Principles Water Potential with Flexible Monomers: Dimer Potential Energy Surface, VRT Spectrum, and Second Virial Coefficient. *J. Chem. Theory Comput.* **2013**, *9*, 5395–5403.

(70) Babin, V.; Medders, G. R.; Paesani, F. Development of a First Principles Water Potential with Flexible Monomers. II: Trimer Potential Energy Surface, Third Virial Coefficient, and Small Clusters. *J. Chem. Theory Comput.* **2014**, *10*, 1599–1607.

(71) Medders, G. R.; Babin, V.; Paesani, F. Development of a First-Principles Water Potential with Flexible Monomers. III. Liquid Phase Properties. *J. Chem. Theory Comput.* **2014**, *10*, 2906–2910.

(72) Reddy, S. K.; Straight, S. C.; Bajaj, P.; Pham, C. H.; Riera, M.; Moberg, D. R.; Morales, M. A.; Knight, C.; Götz, A. W.; Paesani, F. On the Accuracy of the MB-pol Many-Body Potential for Water: Interaction Energies, Vibrational Frequencies, and Classical Thermodynamic and Dynamical Properties from Clusters to Liquid Water and Ice. *J. Chem. Phys.* **2016**, *145*, 194504.

(73) Medders, G. R.; Paesani, F. Infrared and Raman Spectroscopy of Liquid Water through First-Principles Many-Body Molecular Dynamics. *J. Chem. Theory Comput.* **2015**, *11*, 1145–1154.

(74) Medders, G. R.; Paesani, F. Dissecting the Molecular Structure of the Air/Water Interface from Quantum Simulations of the Sum-Frequency Generation Spectrum. *J. Am. Chem. Soc.* **2016**, *138*, 3912–3919.

(75) Straight, S. C.; Paesani, F. Exploring Electrostatic Effects on the Hydrogen Bond Network of Liquid Water through Many-Body Molecular Dynamics. *J. Phys. Chem. B* **2016**, *120*, 8539.

(76) Reddy, S. K.; Moberg, D. R.; Straight, S. C.; Paesani, F. Temperature-Dependent Vibrational Spectra and Structure of Liquid Water from Classical and Quantum Simulations with the MB-pol Potential Energy Function. *J. Chem. Phys.* **2017**, *147*, 244504.

(77) Moberg, D. R.; Straight, S. C.; Paesani, F. Temperature Dependence of the Air/Water

Interface Revealed by Polarization Sensitive Sum-Frequency Generation Spectroscopy. *J. Phys. Chem. B* **2018**, *122*, 4356–4365.

(78) Smith, W.; Forester, T. DL_POLY_2.0: A General-Purpose Parallel Molecular Dynamics Simulation Package. *J. Mol. Graphics* **1996**, *14*, 136–141.

(79) Martyna, G. J.; Klein, M. L.; Tuckerman, M. Nosé-Hoover Chains - The Canonical Ensemble via Continuous Dynamics. *J. Chem. Phys.* **1992**, *97*, 2635–2643.

(80) Nosé, S. A Unified Formulation of the Constant Temperature Molecular Dynamics Methods. *J. Chem. Phys.* **1984**, *81*, 511–519.

(81) Hoover, W. G. Canonical Dynamics: Equilibrium Phase-Space Distributions. *Phys. Rev. A* **1985**, *31*, 1695–1697.

(82) Iuchi, S.; Morita, A.; Kato, S. Molecular Dynamics Simulation with the Charge Response Kernel: Vibrational Spectra of Liquid Water and N-Methylacetamide in Aqueous Solution. *J. Phys. Chem. B* **2002**, *106*, 3466–3476.

(83) Saito, S.; Ohmine, I. Translational and Orientational Dynamics of a Water Cluster $(H_2O)_{108}$ and Liquid Water: Analysis of Neutron Scattering and Depolarized Light Scattering. *J. Chem. Phys.* **1995**, *102*, 3566–3579.

(84) McQuarrie, D. A. *Statistical Mechanics*; University Science Books: Sausalito, CA, 2000.

(85) Londono, J. D.; Kuhs, W. F.; Finney, J. L. Neutron Diffraction Studies of Ices III and IX on Under-Pressure and Recovered Samples. *J. Chem. Phys.* **1993**, *98*, 4878.

(86) Lobban, C.; Finney, J. L.; Kuhs, W. F. The Structure and Ordering of Ices III and V. *J. Chem. Phys.* **2000**, *112*, 7169.

(87) Ludwig, R. Water: From Clusters to the Bulk. *Angew. Chem., Int. Ed.* **2001**, *40*, 1808–1827.

(88) Lobban, C.; Finney, J. L.; Kuhs, W. F. The Structure of a New Phase of Ice. *Nature* **1998**, *391*, 268–270.

(89) OḰeeffe, M. New Ice Outdoes Related Nets in Smallest-Ring Size. *Nature* **1998**, *392*, 879.

(90) Shigenari, T.; Abe, K. Vibrational Modes of Hydrogens in the Proton Ordered Phase XI of Ice: Raman Spectra Above 400 cm^{-1}. *J. Chem. Phys.* **2012**, *136*, 174504.

(91) Gasser, T. M.; Thoeny, A. V.; Plaga, L. J.; Köster, K. W.; Etter, M.; Böhmer, R.; Loerting, T. Experiments Indicating a Second Hydrogen Ordered Phase of Ice VI. *Chemical Science* **2018**, *9*, 4224–4234.

(92) Besson, J. M.; Pruzan, P.; Klotz, S.; Hamel, G.; Silvi, B.; Nelmes, R. J.; Loveday, J. S.; Wilson, R. M.; Hull, S. Variation of Interatomic Distances in Ice VIII to 10 GPa. *Phys. Rev. B* **1994**, *49*, 12540–12550.

(93) Towns, J.; Cockerill, T.; Dahan, M.; Foster, I.; Gaither, K.; Grimshaw, A.; Hazlewood, V.; Lathrop, S.; Lifka, D.; Peterson, G. D. et al. XSEDE: Accelerating Scientific Discovery. *Comput. Sci. Eng.* **2014**, *16*, 62–74.

TOC Graphics